A statistical, physical-based, micro-mechanical model of hydrogen-induced intergranular fracture in steel

P. Novak [a], R. Yuan [b], B.P. Somerday [c], P. Sofronis [a], R.O. Ritchie [b,*]

[a] *Department of Mechanical Science and Engineering, University of Illinois at Urbana-Champaign, 1206 West Green Street, Urbana, IL 61801, USA*
[b] *Department of Materials Science and Engineering, University of California-Berkeley, 216 Hearst Memorial Mining Building, Berkeley, CA 94720-1760, USA*
[c] *Sandia National Laboratories, P.O. Box 969, MS 9403, Livermore, CA 94551, USA*

ARTICLE INFO

ABSTRACT

Intergranular cracking associated with hydrogen embrittlement represents a particularly severe degradation mechanism in metallic structures which can lead to sudden and unexpected catastrophic fractures. As a basis for a strategy for the prognosis of such failures, here we present a comprehensive physical-based statistical micro-mechanical model of such embrittlement which we use to quantitatively predict the degradation in fracture strength of a high-strength steel with increasing hydrogen concentration, with the predictions verified by experiment. The mechanistic role of dissolved hydrogen is identified by the transition to a locally stress-controlled fracture, which is modeled as being initiated by a dislocation pile-up against a grain-boundary carbide which in turn leads to interface decohesion and intergranular fracture. Akin to cleavage fracture in steel, the "strength" of these carbides is modeled using weakest-link statistics. We associate the dominant role of hydrogen with trapping at dislocations; this trapped hydrogen reduces the stress that impedes dislocation motion and also lowers the reversible work of decohesion at the tip of dislocation pile-up at the carbide/matrix interface. Mechanistically, the model advocates the synergistic action of both the hydrogen-enhanced local plasticity and decohesion mechanisms in dictating failure.

© 2009 Elsevier Ltd. All rights reserved.

1. Introduction

It is well recognized that hydrogen represents an abundant, clean and mobile energy carrier. For the hydrogen economy to be fully realized though, efficient hydrogen storage and transportation, for example in high-pressure ($\sim$20–100 MPa) pipelines and pressure vessels, will be essential. A major issue here is the containment of hydrogen, as its presence can lead to a severe degradation in the structural integrity of the containment vessel from a variety of hydrogen-induced/assisted cracking mechanisms, which can result in premature failure. This is especially pertinent to the use of high-strength ferritic steels, which have been identified as low-cost candidate materials for applications such as hydrogen pipelines, pressure vessels and compressors, despite the fact that they can be extremely susceptible to such hydrogen embrittlement.

The effect of hydrogen in degrading the mechanical properties of materials, particularly metals and alloys, is well documented. Hydrogen, either as an external gas, resulting from electrochemical reactions in an aqueous environment, or dissolved in the metal during processing, is known to markedly lower the ductility, fracture strength and fracture toughness, and to accelerate subcritical cracking under sustained and/or cyclic loading. The mechanisms associated with

---

* Corresponding author. Tel.: +1 510 486 5798; fax: +1 510 643 5792.
  E-mail address: roritchie@lbl.gov (R.O. Ritchie).

such degradation in mechanical behavior have remained an issue of contention for many years, but can be broadly classified into three primary mechanisms (Hirth, 1980; Birnbaum et al., 1997), namely (i) *decohesion mechanisms*, where hydrogen at internal interfaces lowers the cohesive strength there ("hydrogen embrittlement"), (ii) *hydrogen-enhanced localized plasticity (HELP)*, where hydrogen affects the local instabilities associated with plastic flow, and in certain material systems, (iii) *hydride formation*, where the presence of highly brittle hydride precipitates results in a "low energy" fracture path. In addition, there are other hydrogen-related degradation mechanisms involving internal gaseous species; these include *blistering*, where high hydrogen concentrations, e.g., associated with electrochemical hydrogen charging, result in the reformation of internal gaseous hydrogen at internal interfaces, leading to high internal pressures and the formation of blistering, and *hydrogen attack*, where at high temperatures and pressures, such internal hydrogen can react with the carbides in steel to form internal methane gas with an associated loss in strength due to decarburization. Although the dominant view is that several of these mechanisms, specifically the decohesion and HELP mechanisms, have been considered to be mutually exclusive, it has been recognized that this may not be the case (Thompson and Bernstein, 1977; Lee et al., 1979; Teter et al., 2001; Gerberich et al., 2009). Indeed, the present work presents a compelling argument that the two mechanisms may in fact be acting in concert.

Despite these many modes of hydrogen-induced degradation, arguably the most devastating is the hydrogen embrittlement of high-strength steels which results in a sharp transition from a high-toughness ductile (microvoid coalescence) fracture to a brittle fracture with an associated dramatic loss in ductility, strength and toughness. Although sometimes associated in quench and tempered steels with transgranular fracture due to the embrittlement of martensite lath and packet interfaces (Lee and Gangloff, 2007), we focus here on the more common transition to hydrogen-induced intergranular fracture associated with diminished decohesion along prior austenite grain boundaries. Specifically, our objective is to quantify this effect of hydrogen on the fracture strength and toughness of a low alloy martensitic steel through the use of a statistically-based micromechanical model for the critical local fracture event which relates the influence of hydrogen adsorbed at internal interfaces in affecting decohesion there to the onset of macroscopic failure.

We model here the process of hydrogen embrittlement in quench and tempered martensitic high-strength steels in terms of intergranular fracture, where it has been shown that cracking follows the prior austenite grain boundaries and crack nucleation is stipulated to occur at decohering carbides or second-phase particles (Kameda and McMahon, 1980; Morgan, 1987; McMahon, 2001). A viable mechanism for such embrittlement is hydrogen-induced decohesion which can account for both the macroscopic embrittlement and the microstructural observations of decohering carbides. Most continuum models of such hydrogen-induced decohesion, however, assume that material failure occurs when a critical hydrogen concentration is attained locally (Akhurst and Baker, 1981; Moody et al., 1990), although this criterion is not based on any well accepted physics nor is it justified on the basis of experimental evidence. Accordingly, we propose here a model of hydrogen-induced intergranular failure in which failure initiates by decohesion at grain-boundary carbide particles with the intensity of the failure event depending on the local stress and hydrogen accumulation associated with a dislocation pile-up at the matrix–carbide interface. Specifically, we employ a weakest-link statistical modeling approach based on Lin et al.'s (1986) statistical adaptation of the RKR model for brittle fracture in steels (Ritchie et al., 1973).

An important input to this weakest-link modeling scheme is the population of such carbide particles within the microstructure with their distribution of differing strengths. The strength of the carbides is inversely related to their size and directly related to the effective fracture work (Curry and Knott, 1978); however, this is critically modulated by the presence of hydrogen in the carbide/matrix interface associated with dislocation pile-ups there. The effective fracture work is estimated from the sum of the reversible work of fracture and the plastic work, following the approach of McMahon et al. (1981). The reversible work of fracture is strongly affected by the presence of hydrogen solutes, in accordance with the thermodynamic model of decohesion of Hirth and Rice (1980). The plastic work for intergranular fracture, which may be a large fraction of the effective fracture work, is assumed to be a function of the reversible work of fracture, following the proposition of Jokl et al. (1980).

We use this statistical micro-mechanical approach to predict the degradation in fracture strength in a high-strength low alloy steel as a function of hydrogen concentration, where the concentrations are specified with some precision by using thermal precharging methods in hydrogen gas, accurately applying thermodynamic relationships for hydrogen content and distribution, and accounting for hydrogen content transients due to time-varying hydrogen gas pressure and temperature. The key features of our approach are the development of a comprehensive statistical micro-mechanical yet physics-based model, we identify a new controlling step in micro-mechanistic events that leads to intergranular fracture in the presence of hydrogen, and we use computational modeling to predict the concentration of trapped hydrogen as a function of history. We believe that this methodology could form the basis for an efficient hydrogen-induced fracture prognosis procedure (Gangloff, 2009) to monitor evolution of damage and the onset of fracture instability for components subjected to exposure from hydrogen gas.

2. Experimental and numerical procedures

An air-melted, low alloy, high-strength AISI 4340 steel (see Table 1) heat treated in the austenitized (870 °C, 1 h), oil quenched, and tempered (200 °C, 2 h) condition to an Rc hardness of 53, was used for the experiments, which were performed on electric discharge machined single- and double-notched bend and 25.4-mm gauge dog-bone tension

Table 1
Chemical composition (wt%) of AISI 4340 steel.

Element	C	Mn	P	S	Si	Cu	Ni	Cr	Mo	Al	V	N	Nb	Sn	Fe
wt%	0.41	0.75	0.012	0.007	0.22	0.16	1.71	0.82	0.21	0.027	0.003	0.0062	0.001	0.007	Bal

specimens. The notched specimens were 6.4-mm thick, 12.7 mm wide and 101.6 mm long. The uncracked ligament was 8.47 mm, the notch angle 22.5°, and the notch root radius was 0.25 mm.

Samples to be thermally precharged in hydrogen gas were first electroplated (30 min at 43 °C at a current density of 1085 A/m^2) with 4–10 µm-thick copper to create an insulating layer for minimizing hydrogen loss at room temperature, and then baked *in vacuo* (150 °C, 24 h) to remove any hydrogen that was introduced during electroplating. Subsequent thermal precharging in hydrogen gas was conducted in an autoclave at 100 °C for a duration of 2 weeks under four different pressures: 138, 69, 34.5 and 6.9 MPa.

One advantage that thermal precharging in hydrogen gas provides over other hydrogen exposure methods (e.g., electrochemical precharging) is the opportunity to accurately apply thermodynamic relationships to calculate hydrogen content and distribution in the material. For example, the concentration of hydrogen in the lattice, C_L, can be readily calculated from Sievert's law (i.e., $C_L = K\sqrt{f}$, where K and f are solubility and fugacity, respectively), since the hydrogen fugacity is easily determined from measured pressure. The concentration of hydrogen in trap sites can also be calculated, provided the trap binding energies and trap site densities are known. For the 4340 steel in this study, trap binding energies were determined using thermal desorption analysis (TDA) (Sofronis et al., 2009). Details of the procedures and analysis from the TDA experiments are provided in Appendix A.

At the end of the 2-week hydrogen charging period, hydrogen residing at normal interstitial lattice sites (NILS) was assumed to be in equilibrium with hydrogen gas as dictated by Sievert's law, and consequently the hydrogen concentration was uniform in the specimens. The associated occupancy of the trapping sites was calculated by Oriani's theory (1970). In view of the high mobility of hydrogen solute atoms in bcc steel and the inability of the thin copper surface layer to function as a perfect insulator, hydrogen outgassed from the specimens during gradual cooling from the charging temperature in the autoclave and after removal from the autoclave. Finite element simulation of the outgassing process was performed to determine the remnant hydrogen concentration in both NILS and trapping sites as a function of gas pressure and temperature history in order to determine this hydrogen concentration just prior to loading of each specimen. The details of the outgassing calculations are stated in Appendix B. During loading of the specimens, internal hydrogen redistribution was dictated by chemical potential gradients qualified by hydrostatic stress gradients and changing demands for trapping, as dislocation traps were generated by plastic straining. The calculated local hydrogen concentrations were used to determine the cohesive strength of the carbide/matrix interface.

One set of hydrogen-charged SE(B) (single edge notched bend) specimens was intentionally outgassed for 18 days at room temperature prior to mechanical testing. The purpose of these tests was to allow hydrogen to desorb from lattice sites and low-binding energy trapping sites in order to assess the hydrogen population that governs fracture strength.

All mechanical testing was performed under displacement control on an automated servo-hydraulic testing machine (MTS 310, MTS Corporation, Eden Prairie, MN, USA) within 2–3 days of charging (to minimize hydrogen loss). Constitutive behavior was obtained from the uniaxial tensile tests (performed in accordance with ASTM Standard E-8). Nominal fracture strength values were determined from the SE(B) tests as a function of hydrogen concentration. They were computed in terms of the nominal bending stress, $\sigma_{nom} = 6Fz/Ba^2$ where B is the thickness, F the applied force, z the moment arm and a the uncracked ligament. The nominal stress denotes the maximum bending stress in a straight beam of height a. The double-notched specimens were tested in the 138 MPa hydrogen-charged and uncharged states in four-point bending to identify the critical local fracture events. As both notches experience the same bending moment, in principle both should fail simultaneously; however, one notch invariably fails leaving the other "frozen" at the point of fracture. By examining the microstructure in the vicinity of the root of the unbroken notch, it is generally possible to identify precursor (local) microscopic events prior to fracture, e.g., failed particle interfaces, microcracked grains, etc., and to discern whether the fracture events are locally stress- or strain-controlled. Such experiments were also conducted on interrupted single-notched samples, where the test was stopped at the onset of fracture, again to discern the location of the initial fracture events.

Extremely slow loading rates were used to allow for internal hydrogen redistribution during testing; specifically, the bend tests were conducted at a displacement rate of 0.1 µm/s, the uniaxial tensile tests at 0.5 µm/s.[1]

Microstructures were examined with optical and scanning (SEM) and transmission (TEM) electron microscopy, using quantitative metallography to measure prior austenite grain size (d) and carbide size (l) distributions; in addition, energy dispersive X-ray analysis was employed to discern inclusion and grain-boundary compositions. Two separate etchants were used: 2% Nital solution (3 s) to image the matrix (lath martensite/carbide) microstructure, and a picral solution (70 °C, 90 s)

---

[1] Our numerical simulations revealed that imposed macroscopic displacement rates of 0.1 µm/s produce local plastic strain rates at the notch root that do not exceed 10^{-4} s^{-1}. Strain rates of this order of magnitude are slow enough for plasticity-mediated hydrogen embrittlement to occur (Birnbaum and Sofronis, 1994).

to reveal the prior austenite grain size. For TEM measurements of the carbide size distribution, specimen foils were polished to 120 μm thick, electropolished in a solution of 50 mL perchloric acid and 450 mL acetic acid for 3 min. Carbide size statistics were based on measurements on more than 100 carbide particles in six TEM images from two separate specimens. Corresponding fractography was performed using scanning electron microscopy operating in the secondary electron mode.

3. Microstructural and mechanical test results

The tempered martensitic microstructure (Nital etched) of the quenched and tempered AISI 4340 steel is shown in Fig. 1. SEM imaging and X-ray diffraction studies indicated that no significant microstructural changes occurred with hydrogen charging. The prior austenite grains, revealed by picral etching (Fig. 1a), had an average size of 10.1 ±4.2 μm, and contained needle-like grain-boundary carbides, with a mean length of 0.61 ±0.36 μm; the carbide size distribution is shown in Fig. 1d. A small fraction of largely MnS inclusions (sized ~1–10 μm) was also sparsely distributed throughout the matrix.

The TDA method applied to both hydrogen-charged and uncharged 4340 steel revealed three hydrogen trap sites having binding energies equal to 18, 48 and 72 kJ/mol (see Appendix A). The trap site having a binding energy of 18 kJ/mol is associated with the elastic strain field of dislocations and the other two trap sites (binding energies of 48 and 72 kJ/mol) primarily with interfaces. Although several types of incoherent interfaces including prior austenite grain boundaries could account for the trap site with binding energy equal to 48 kJ/mol, the higher-energy trap site with binding energy equal to 72 kJ/mol is likely associated with carbide/matrix interfaces (see Appendix A). The density of trap sites was chosen as follows: (i) for the dislocations, we assumed the trapping model of Kumnick and Johnson (1980) in which the density of traps evolves with plastic straining. For an undeformed sample, the density of the dislocation trap sites is 8.5×10^{20} m^{-3}; (ii) for the grain boundaries and the carbides, we adopted the values given by Hirth (1980), that is, 10^{23} and 5×10^{24} m^{-3}, respectively. To validate these choices, we measured through thermal desorption analysis the hydrogen content of undeformed samples charged at pressure 97 MPa and temperature 85 °C for 210 h (see Appendix A). Our calculation of the equilibrium hydrogen content, both in the lattice and the traps matched the experimental result. The details are given in Appendix B.
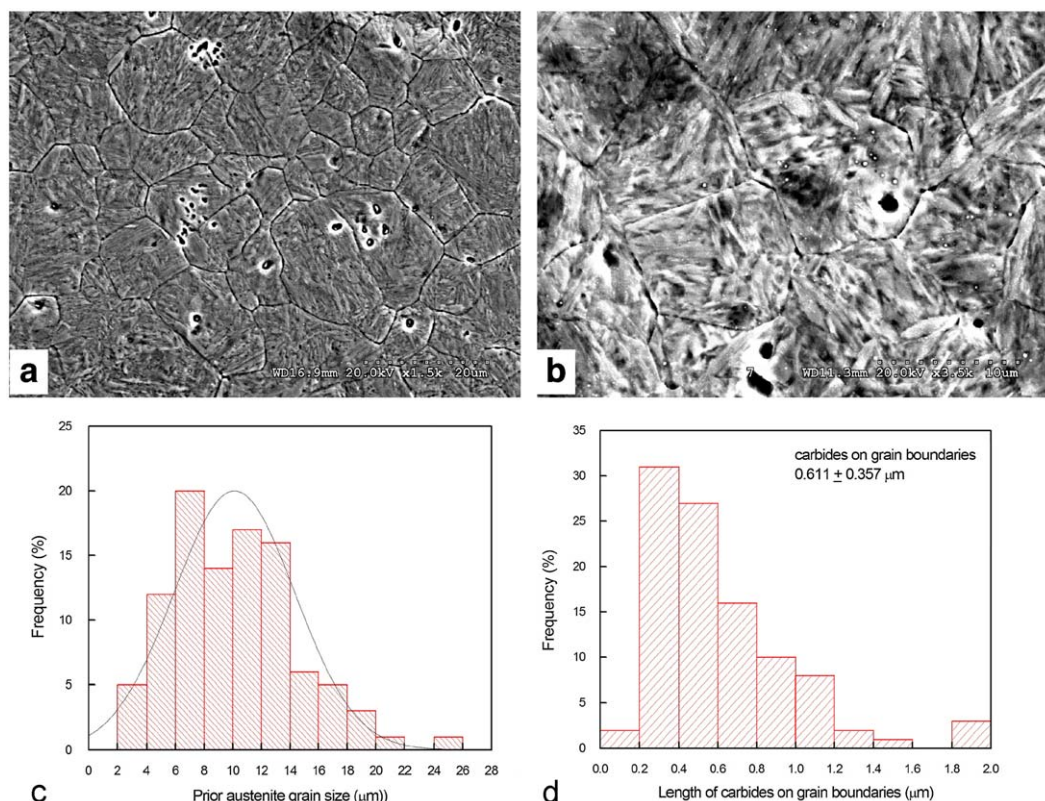

Fig. 1. Microstructure of the quenched and 200 °C tempered AISI 4340 steel, showing scanning electron micrographs of (a) prior austenite grains (etchant: modified Winsteard's reagent at 65 °C for 90 s), and (b) the morphology of inclusions and carbides on grain boundaries, and the quantitative size distributions of the (c) prior austenite grains and (d) grain-boundary carbides. Statistical information on the size of the carbides was taken from high-resolution transmission electron micrographs based on measurements of more than 100 carbide particles in six TEM images from two separate specimens.
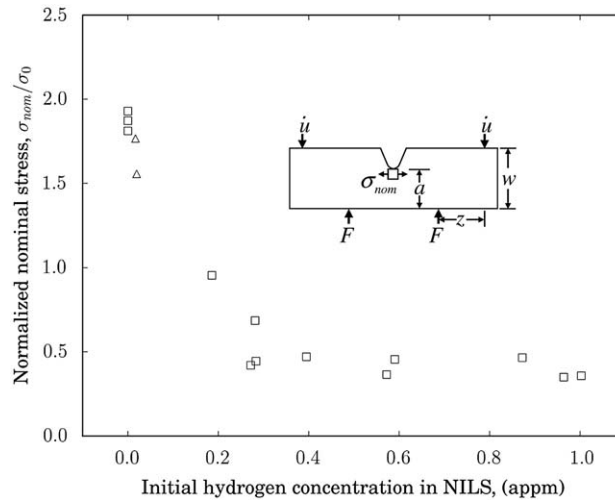
Fig. 2. Variation in fracture (normalized nominal bending stress) with hydrogen concentration in the specimen upon the initiation of loading at a displacement rate of $\dot{u} = 0.1$ μm/s. The nominal bending stress $\sigma_{nom} = 6Fz/Ba^2$ denotes the maximum bending stress in a straight beam of thickness B, uncracked ligament a, under the same force F and moment arm z. The yield stress in uniaxial tension is σ_0=1490 MPa. Samples that were outgassed for 18 days at room temperature are denoted by the triangular data-points.

Uniaxial tensile test results for the uncharged and hydrogen-charged conditions revealed yield and tensile strengths in the uncharged steel of, respectively, 1490 and 1760 MPa. The constitutive behavior remained essentially unchanged with hydrogen, except for the fact that with increasing hydrogen concentration, the samples fractured progressively earlier along the stress–strain curve.

The corresponding variation in fracture strengths with hydrogen charging conditions, in the form of the nominal four-point bending strengths, reveals a dramatic reduction in strength (by a factor of ∼5) with increasing lattice hydrogen concentration (Fig. 2). This was accompanied by a fracture mode change from a ductile microvoid coalescence fracture in the uncharged steel to brittle intergranular fracture with hydrogen (Fig. 3). Double- and single-notched bend testing clearly revealed that whereas *ductile fracture* in the uncharged steel is *strain-controlled* as the fracture initiated directly at the notch root where the local strains are highest (Fig. 3a), the local fracture event for the initiation of *brittle fracture* in the presence of hydrogen is *stress-controlled* as the fracture initiated ahead of the notch root, typically near the elastic–plastic interface where the local tensile stresses are highest (Fig. 3b). From metallographic examination, this local crack initiation event for hydrogen-induced intergranular fracture appeared to be associated microstructurally with the interface cracking of a needle-like grain-boundary carbide. This is perfectly in accord with the scenario proposed for intergranular embrittlement in martensitic alloy steels (Kameda and McMahon, 1980; Kameda and McMahon, 1983; Morgan, 1987; McMahon, 2001).

The plot of fracture strength vs. lattice hydrogen concentration in Fig. 2 includes results for the two SE(B) specimens that were intentionally outgassed for 18 days at room temperature prior to mechanical testing. As observed in the plot, the fracture strength of these outgassed specimens was nearly equal to the strength of the uncharged specimens. Finite element simulation of the 18-day outgassing process (Appendix B) demonstrated that hydrogen completely desorbed from both lattice sites and the trap site having the lowest binding energy (18 kJ/mol). Furthermore, the simulations revealed that the two trap sites with higher binding energies (48 and 72 kJ/mol) remained saturated with hydrogen (over 99% trap occupancy). The latter results, indicating the propensity for the high-binding energy trap sites to retain hydrogen, are supported by TDA results from the uncharged steel (see Appendix A). These TDA spectra showed that the uncharged steel had significant amounts of hydrogen residing *only* in the two high-binding energy trap sites. The collective results from tests on the intentionally outgassed SE(B) specimens and calculations of the outgassing process indicate the relative importance of hydrogen in the lattice and low-binding energy sites vs. hydrogen in the high-binding energy sites. Specifically, fracture in the hydrogen-charged steel is not governed by the high-binding energy trap sites because these sites (e.g., interfaces) remain saturated with hydrogen, independent of loading and/or hydrogen exposure conditions; rather, it is dependent on the lattice sites and low-binding energy trap sites where the hydrogen concentration is a function of time and loading.

4. Theoretical fracture model

With the mechanistic role of hydrogen deemed to be associated with the transition to a locally stress-controlled (nominally) brittle intergranular fracture, which is modeled by an interface crack in a grain-boundary carbide ahead of the notch tip, we can now construct a statistically-based micromechanical model for this process. The carbide particles are thus considered to be subject to cracking/decohesion along the particle–matrix interface, an event affected by the hydrogen
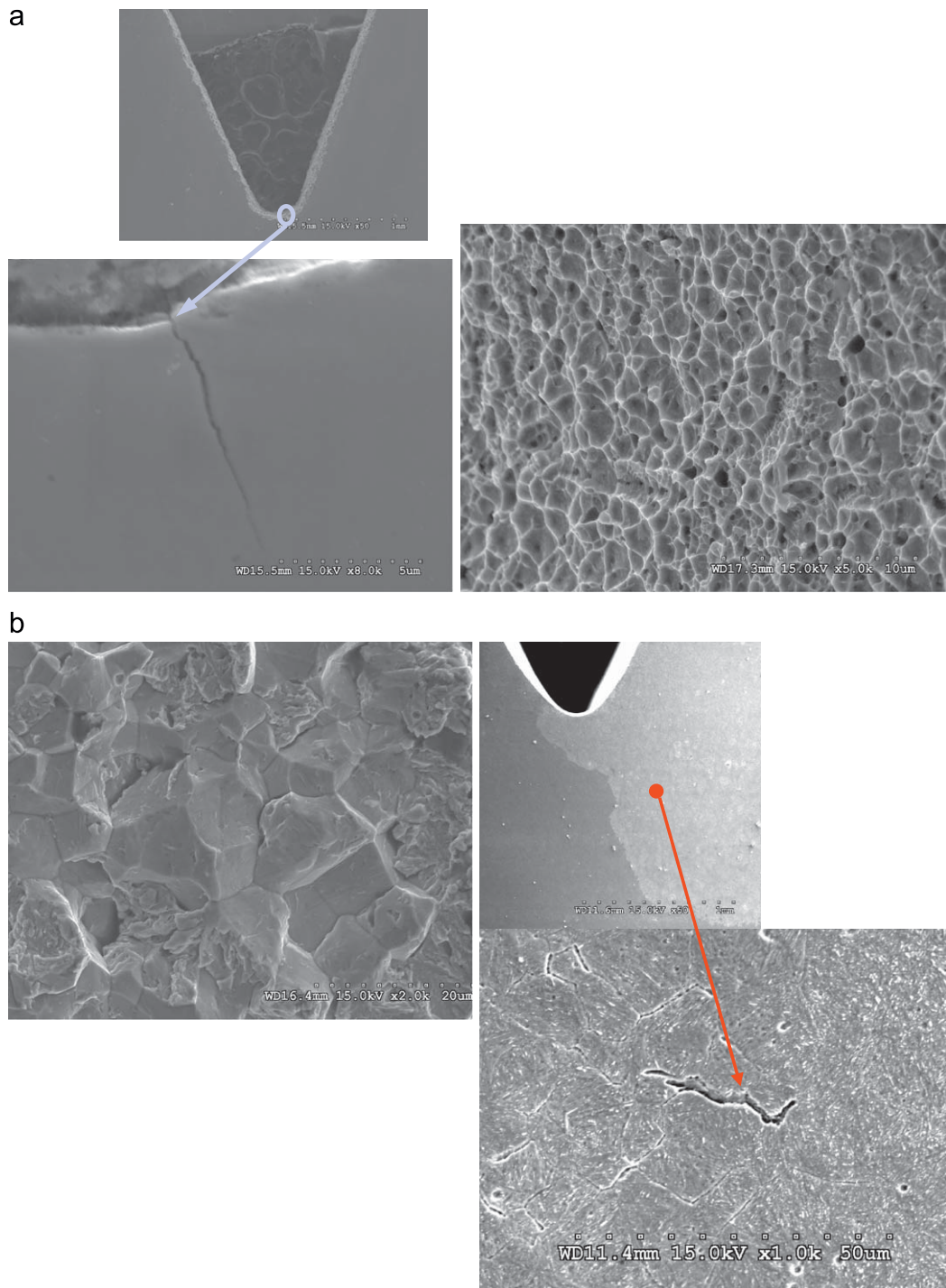
Fig. 3. Scanning electron micrographs of double-notched AISI 4340 steel specimens showing (a) strain-controlled ductile fracture associated with microvoid coalescence initiating at the notch in a non-charged sample, as compared with (b) stress-controlled brittle fracture associated with intergranular cracking initiating ahead of the notch in a 138 MPa hydrogen-charged sample.

concentration there which is considered to reduce cohesion with the resultant cracks treated as non-interacting flaws capable of inducing fracture upon propagation under decreasing load. Akin to cleavage fracture in steel (Lin et al., 1986), we accordingly apply a weakest-link statistical approach. Weakest-link statistics dictate that the microstructure ahead of the notch tip be divided into volume elements of the material, of size dV, that are subject to a constant stress σ; each of

these elements has an (elemental) failure probability, $d\phi$, given by

$$d\phi = dV \left(NN_T^{(c)} \int_0^\sigma g(S)dS \right), \tag{1}$$

where N is the fraction of the number of particles per unit volume $N_T^{(c)}$ that participate in the decohesion process and the integral denotes the fraction of particles with strength S less than σ (as dictated by the Poisson postulate). The total failure probability of the entire structure, Φ, can then be estimated by noting that the total survival probability $(1-\Phi)$ is given by the product of all the elemental survival probabilities:

$$1 - \Phi = \Pi(1 - d\phi) = \exp[-NN_T^{(c)} \int_0^V \int_0^\sigma g(S)dSdV] \tag{2}$$

where σ denotes a single component (e.g., maximum principal stress) of the local stress tensor σ_{ij}. For a sample loaded under plane-strain conditions, the volume dV of an element can be considered as (Lin et al., 1986)

$$dV = 2b \int_0^\pi r \, dr \, d\theta, \tag{3}$$

where b relates to the width of the sample and (r, θ) are polar coordinates centered at the notch tip.

Results summarized in the previous section, i.e., fracture strength measurements on SE(B) specimens that were hydrogen charged then intentionally outgassed coupled with calculations of the outgassing process, indicate that fracture in the hydrogen-charged steel is not governed by the high-binding energy trap sites (assumed to be grain boundaries and carbide/matrix interfaces) but rather the lattice sites and low-binding energy trap sites (assumed to be dislocations). Furthermore, as discussed in the next section, the grain boundaries and carbides were fully saturated with hydrogen (occupancies greater than 99%), not only at the beginning of testing but during the entire test duration for all charged specimens regardless of the hydrogen charging pressure. We therefore conclude that hydrogen residing at the carbide/matrix interface or at grain boundaries cannot be the responsible controlling step for the failure event which, as shown in Fig. 2 exhibits a dependence on the amount of hydrogen in the specimen, i.e., the failure stress decreases as the concentration at the beginning of testing increases. Thus, we conclude that failure by decohesion at the carbide/matrix interface is associated with the low-binding energy trap site, i.e., dislocations. The hydrogen population at dislocations varies during loading of the specimen toward failure, as hydrogen redistributes from NILS to dislocation traps. In particular, we model that fracture occurs by the impingement on the carbide/matrix interface of a dislocation pile-up, as depicted in Fig. 4, consistent with the proposed scenario for intergranular hydrogen embrittlement in martensitic steels (Kameda and McMahon, 1980, 1983; Morgan, 1987; McMahon, 2001). The hydrogen trapped at the dislocations reduces the stress that impedes dislocation motion, thus increasing the number of dislocations in the pile-up. Also, hydrogen trapped at the dislocations reduces the reversible work of decohesion of the carbide/matrix interface if one considers the interface to be embedded within the dislocation atmosphere. As mentioned in the introduction, the reduction of the reversible work of decohesion is associated with a corresponding reduction of the plastic work accompanying decohesion.

The distribution of strengths S of the particles can be deduced from the carbide particle size distribution for the 4340 steel shown in Fig. 1d. Based on the fracture model described in the preceding paragraph, we deduce the strengths S of the particles from the carbide size, l, distribution through the Smith (1966) model, viz:

$$\frac{l}{d}S^2 + \tau_{eff}^2 \left[1 + \frac{4}{\pi} \frac{\tau_0}{\tau_{eff}} \sqrt{\frac{l}{d}} \right]^2 = \frac{4E\gamma_{eff}}{\pi(1 - \nu^2)d}, \tag{4}$$
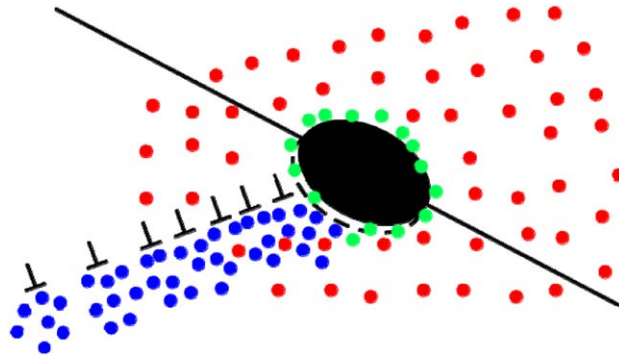

Fig. 4. Mechanistic steps in the generation of intergranular fracture in the presence of hydrogen. Schematic showing a dislocation pile-up impinging on a grain-boundary carbide, leading to decohesion at a carbide/matrix interface and in turn intergranular fracture. Hydrogen atoms are denoted by colored circles: blue for hydrogen carried by the dislocations, green for hydrogen trapped at the carbide, red for hydrogen at normal interstitial lattice sites.
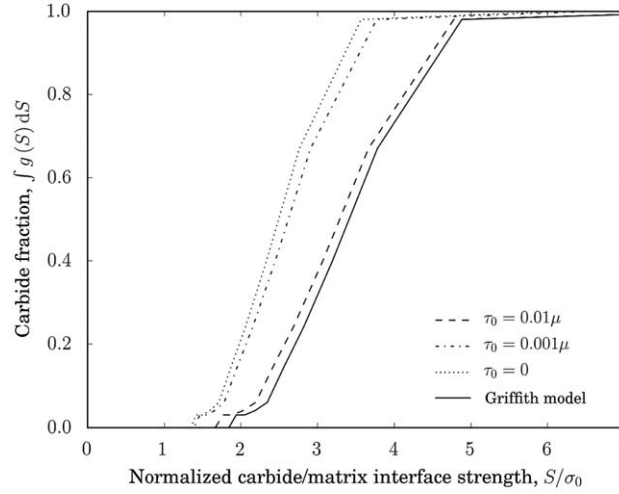
Fig. 5. Cumulative carbide strength distribution calculated through Eq. (4) for the Smith model under shear stress τ_Y=860 MPa and various values of the stress τ_0 resisting dislocation motion. Superposed on the figure is the distribution according to a Griffith model, $S = \sqrt{\pi E \gamma_{eff}/(1-v^2)l}$, for pure transgranular cleavage (Lin et al., 1986), where l is the carbide particle size.

where E is the Young's modulus, v is Poisson's ratio, d is the grain diameter, τ_0 is the stress resisting dislocation motion, τ_{eff} is an effective stress equal to the difference between the applied shear stress τ_Y and the stress τ_0, $\tau_{eff} = \tau_Y - \tau_0$, and γ_{eff} is the effective work of decohesion of the carbide/matrix interface which is a function of the hydrogen solute atoms carried by the dislocations.[2] In the statistical model of Lin et al. (1986), brittle failure of a low-strength ferritic steel was triggered by cracking of grain-boundary carbide particles (analyzed using a Griffith model, where $S = \sqrt{\pi E \gamma_{eff}/(1-v^2)l}$), leading to transgranular cleavage fracture of the adjacent grain. This failure model, which provided reliable predictions of the critical stress-intensity factor, K_{IC}, for failure, was based on an effective fracture work of $\gamma_{eff} = 23\,\mathrm{J\,m^2}$. Lacking such measurements for a quenched and tempered steel, this value, which describes the elasto-plastic work for fracture that accompanies carbide cracking and the associated plastic dissipation upon crack propagation in a ferritic steel, is assumed in the present work for failure *in the absence of hydrogen*. For such an effective fracture work and an applied shear stress $\tau_Y = \sigma_0/\sqrt{3} = 860$ MPa, the cumulative particle strength distribution in the absence of hydrogen, can be deduced from the particle size distribution in Fig. 1d using Eq. (4), and is shown in Fig. 5. It is seen that as the stress opposing the dislocation motion τ_0 increases, the estimated strength of the particle/matrix interface increases. This relates to the formation of pile-ups with fewer dislocations due to the increased obstacle strength, and hence extra load is required to accumulate enough dislocations in the pile-ups to accentuate the effective stress and bring about decohesion at the interface. Thus, much higher stresses are required to debond the particles in the Griffith model than in the Smith model. We therefore expect that hydrogen, by shielding the interaction between dislocations,[3] decreases the obstacle strength and that this results in a decreased interfacial cohesive strength. In addition, hydrogen further lowers the strength of the interface by simultaneously reducing the effective work of fracture. We observe that the present model advocates a synergistic action of the HELP and decohesion mechanisms in bringing about material failure.

Hydrogen is considered to reside at either NILS or trapping sites at carbides, grain boundaries, and dislocations. The trapping site occupancies for carbides, $\theta_T^{(c)}$, for grain boundaries, $\theta_T^{(gb)}$, and for dislocations, $\theta_T^{(d)}$, are always in equilibrium with the lattice site occupancy θ_L according to Oriani's theory (1970):

$$\frac{\theta_T^{(j)}}{1-\theta_T^{(j)}} = \frac{\theta_L}{1-\theta_L}\exp\left(\frac{W_B^{(j)}}{RT}\right), \tag{5}$$

where the superscript j denotes any of (c, gb, d), $W_B^{(j)}$ is the binding energy of hydrogen to the corresponding traps, R is the gas constant equal to $8.31\,\mathrm{J\,mol^{-1}\,K^{-1}}$, and T is the absolute temperature. The hydrogen concentration in NILS is given by $C_L = \beta N_L \theta_L$, where $N_L = N_A/V_M$ denotes the number of solvent atoms per unit volume, V_M is the molar volume of the host lattice, N_A is Avogadro's number and β is the number of interstitial sites per solvent atom. The hydrogen concentration in trapping sites is calculated through $C_T^{(j)} = \alpha^{(j)} N_T^{(j)} \theta_T^{(j)}$, where $\alpha^{(j)}$ denotes the number of trapping sites per trap of type (j), and

---

[2] The form of the Smith model used here incorporates the Hall–Petch relationship to justify the reciprocal grain-size dependency of yield strength in the second term in Eq. (4).

[3] Although the notion of dislocation shielding in a complex microstructure such as tempered martensite may appear questionable, it should be noted that the HELP mechanism has been experimentally observed to operate in a wide variety of engineering alloys, including bcc steels (Robertson, 2001).

$N_T^{(j)}$ is the corresponding trap density. The trap density at dislocations $N_T^{(d)}$ increases with plastic straining, whereas the carbide trap density $N_T^{(c)}$ and grain-boundary trap density $N_T^{(gb)}$ remain constant. The hydrogen transport equation[4] accounting for stress-driven diffusion and trapping at all three trapping sites is described by (Sofronis and McMeeking, 1989)

$$\frac{D}{D_{eff}}\frac{\partial C_L}{\partial t} = DC_{L,ii} - \left(\frac{DV_H}{3RT}C_L\sigma_{kk,i}\right)_{,i} - \left(\sum_j \alpha^{(j)}\theta_T^{(j)}\frac{\partial N_T^{(j)}}{\partial \varepsilon^p}\right)\frac{\partial \varepsilon^p}{\partial t}, \tag{6}$$

where $()_{,i} = \partial()/\partial x_i$, $\partial/\partial t$ denotes partial differentiation with respect to time t, ε^p is the effective plastic strain, D_{eff} is an effective diffusion coefficient related to the NILS diffusion coefficient D through

$$\frac{D}{D_{eff}} = 1 + \sum_j \frac{\partial C_T^{(j)}}{\partial C_L}, \tag{7}$$

and the standard summation convention is implied over a repeated index that is not enclosed in parentheses.

Hydrogen is assumed to affect the reversible work of decohesion $2\gamma_{int}$ (also called the ideal work to fracture), as described by the Hirth and Rice (1980) thermodynamic theory of decohesion; for the case of fast decohesion:

$$2\gamma_{int} = (2\gamma_{int})_0 - (\Delta g_i - \Delta g_s)\Gamma = 2\gamma_s - \gamma_i - (\Delta g_i - \Delta g_s)\Gamma, \tag{8}$$

where $(2\gamma_{int})_0$ is the reversible work of decohesion in the absence of hydrogen, $2\gamma_s$ and γ_i are, respectively, the free surface and carbide/matrix interface energies in the absence of hydrogen, Δg_i and Δg_s are, respectively, the Gibbs free energy excesses when hydrogen is absorbed onto the particle/matrix interface and the free surface created upon separation and Γ is the interface coverage by hydrogen measured in hydrogen solute atoms per unit area. The effective decohesion work γ_{eff} in Eq. (4) is the sum of the reversible work of decohesion $2\gamma_{int}$ and the plastic work γ_p accompanying the decohesion initiation event, $\gamma_{eff} = 2\gamma_{int} + \gamma_p$. In elegant studies of microcrack propagation, McMahon and Vitek (1979) and Jokl et al. (1980) determined the dependence of the plastic work expended upon microcrack propagation on the reversible work of fracture upon propagation. The segregation of hydrogen to carbide/matrix interfaces not only reduces the reversible work of decohesion as dictated by Eq. (8), but also greatly reduces the attendant plastic work. The sensitivity of the predicted fracture strength to this relationship between the plastic work and the reversible work to fracture must be investigated through parametric studies because the appropriate form for this relation is unknown. Following Jokl et al. (1980), we adopt the form

$$\gamma_p = A(2\gamma_{int})^q, \tag{9}$$

where A calibrates the magnitude of the plastic work and q magnifies the effect of changes in the reversible work to fracture on the plastic work. The calibration is carried out such that in the absence of hydrogen the reversible work of decohesion is $(2\gamma_{int})_0$ and the effective fracture work is equal to 23 J/m^2, a value used by Lin et al. (1986) as representing the magnitude of the reversible work of fracture of carbide particles in a ferritic steel. In the presence of hydrogen, the effective work of decohesion decreases to its minimum when the reversible work of decohesion decreases to its minimum.

The hydrogen atmosphere around carbide particles that causes interfacial decohesion comprises the hydrogen trapped at the carbides, which as noted above are saturated in our continuum model of trapping,[5] the hydrogen deposited by the impinging dislocation pile-up, and the hydrogen in the surrounding normal interstitial lattice sites. The interaction of the pile-up and carbide stress fields alters the capability of the interface to accommodate hydrogen both through the stress field superposition and the local distortion of the atomic nature of the interface. Thus, accurate accounting of the amount of hydrogen around a single carbide particle would require a micro-mechanical model in which parameters such as modulus and size of the particle would need to be included. Due to the absence of such a robust model, we assume here that the occupancy of the interface is equal to the occupancy of the dislocation trap sites, $\theta_T^{(d)}$, as furnished by the solution of Eq. (6). This assumption is compatible with our decohesion model whereby the interface is embedded in the dislocation atmosphere. Thus, this model for the interfacial hydrogen coverage Γ is as follows:

$$\Gamma = \eta \theta_T^{(d)} \Gamma_{max}, \tag{10}$$

where Γ_{max} denotes the number of trapping sites per unit area of the carbide/matrix interface and η is a multiplicative factor, set by parametric studies to be 0.01, that reflects the fact that not every impinging dislocation pile-up participates in the decohesion process. In addition, we determine Γ_{max} by considering the relationship $\alpha^{(c)} = \Gamma_{max}\sum \pi l_i^2 f_i$ for the total number of trapping sites per carbide particle in which l_i and f_i denote, respectively, the carbide size and the associated frequency as shown in Fig. 1d. Given $\alpha^{(c)} = 9.09 \times 10^{12}$ trapping sites per carbide (see Appendix B), we find $\Gamma_{max} = 6.17 \times 10^{24}$ interfacial trapping sites/m^2 of carbide/matrix interface. Although approximate, this approach leads to excellent macroscopic fracture stress predictions.

---

[4] We neglected the convective term from the hydrogen transport equation (Varias, 2007) because our finite element calculations show that, when included, it has no effect on the results.

[5] We note that the continuum model does not address the material and geometric details of the particles, such as modulus and shape.
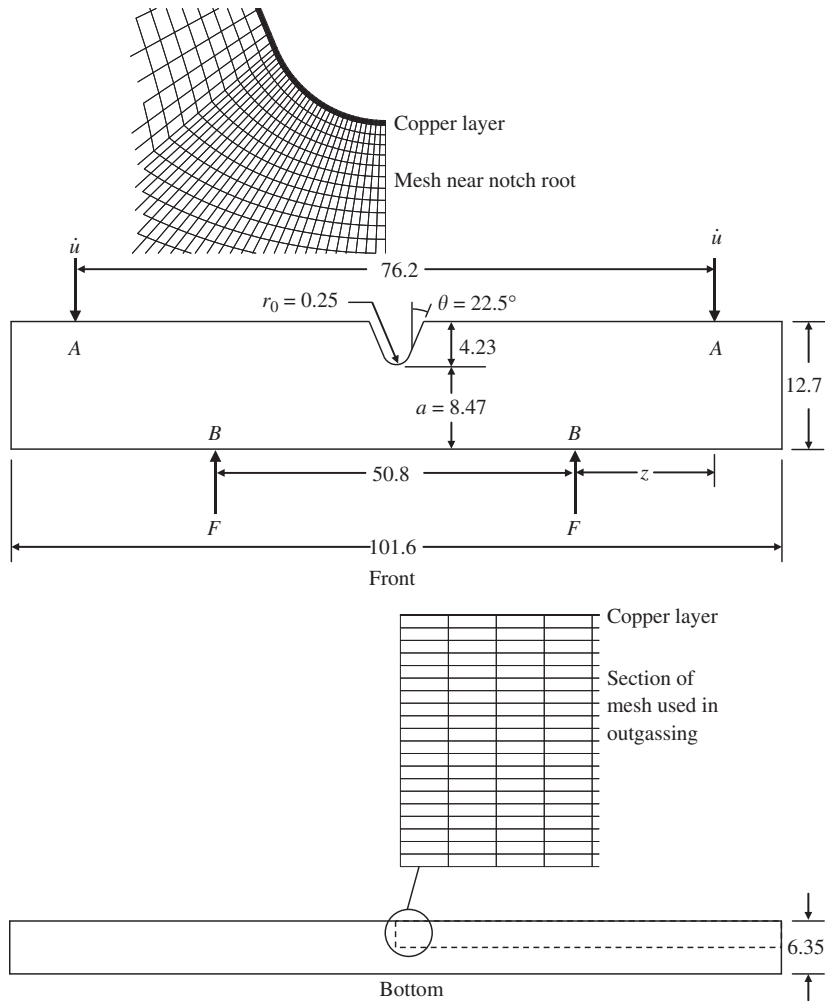
Fig. 6. Finite-element numerical model of the single edged-notched four-point bend specimen used in the fracture studies. All dimensions are in millimeters.

5. Modeling results

Cumulative failure probabilities for the entire structure were found by integrating Eq. (2) over the entire modeling domain. At each integration station of each element in the finite element discretization, the stress σ was determined by the finite element method, which allowed for the calculation of the number of particles per unit volume $NN_T^{(c)} \int_0^\sigma g(S)dS$ with a strength less than σ. For the fraction N of particles per unit volume that participate in the decohesion process, 5% of the number of particles are taken as measured per unit volume[6] (Fig. 1d). The applied boundary displacements were incremented until the failure load was reached, when the total failure probability was equal to one-half, $\Phi = 0.5$.

A schematic of the modeled domain, a single-edge notched SE(B) specimen, is shown in Fig. 6. The specimen dimensions were identical to the experimental test samples, i.e., 101.6 mm long with thickness $B = 6.4$ mm, width $W = 12.7$ mm, uncracked ligament $a = 8.47$ mm, moment arm $z = 12.7$ mm, undeformed notch radius $r_0 = 0.25$ mm and notch angle $\theta = 22.5°$; the outer and inner loading spans were, respectively, $L_o = 76.2$ mm and $L_i = 50.8$ mm. These specimens were loaded at a displacement rate $\dot{u} = 0.1\,\mu\text{m/s}$ at points A and B had no vertical displacement. Due to symmetry only half the specimen was modeled; the symmetry line ahead of the notch root was prescribed to have zero shear traction and horizontal displacement, and was impermeable to hydrogen (zero flux). The outer boundary of the specimen was prescribed to have zero hydrogen concentration allowing for continued hydrogen outgassing during loading. The initial

---

[6] This number represents the portion of carbide particles engaged in the fracture process. It is a value which is essentially impossible to measure but we use 5% here as this was the fraction used in the statistical model of Lin et al. (1986) which was consistent with the predicted and measured fracture toughnesses for transgranular cleavage fracture. Parametric studies indicate that this 5% value best describes the trend in the experimental data as the initial NILS hydrogen concentration at the beginning of testing increases.

hydrogen concentration throughout the domain at time $t=0$, just before loading, was found by simulating the hydrogen outgassing from the moment the specimen was taken out from the charging furnace till it was placed in the loading device. The details for this calculation of the initial hydrogen concentration are given in Appendix B. For the computations, a mesh with 5985 elements was used. The experimentally measured uniaxial stress–strain curve was modeled through

$$\sigma_Y = \sigma_0 \left(1 + E\frac{\varepsilon^p}{\sigma_0}\right)^{1/n},$$ (11)

where the yield stress $\sigma_0 = 1490$ MPa, the Young's modulus $E = 200$ GPa, Poisson's ratio is 0.3, and the strain-hardening exponent $n = 7.7$. The material was assumed to obey the von Mises yielding criterion with the associated flow rule. The coupling of the hydrogen transport problem with the material elastoplastic deformation followed the approach documented by Sofronis and McMeeking (1989) and Liang and Sofronis (2003).

Unless otherwise stated, the finite element calculations were carried out assuming the Kumnick and Johnson (1980) model for the evolution of the trap density $N_T^{(d)}$ at dislocations (Taha and Sofronis, 2001); in addition, $\tau_0 = 76.9$ MPa for the stress resisting dislocation motion in the Smith model of Eq. (4), $A = 0.0216$ and $q = 6$ in Eq. (9) for the relationship between plastic and reversible work for decohesion, with $\dot{u} = 0.1$ μm/s for the displacement rate of the specimens. The assumed values for A and q yield a nonlinear curve similar to that proposed by Jokl et al. (1980). The values of the material parameters that were used to describe hydrogen-induced decohesion through Eq. (8) are listed in Table 2. The values for the rest of the material parameters, such as the molar volume, etc., are listed in Table 3. Since loading of the specimens was carried out at room temperature, the diffusion coefficient through normal interstitial lattice sites was taken to be $D = 1.5 \times 10^{-8}$ (m²/s) (Nelson and Stein, 1973).

Fig. 7 shows the results of one such computation in the form of contour plots at the moment of specimen failure of (a) the maximum principal stress σ_1 that represents the strength of the particle/matrix interface, (b) the effective stress that is responsible for the pile-up formation and thereby affects the magnitude of the particle/matrix interface strength as dictated by the Smith model, (c) the occupancy of the sites for hydrogen trapped at dislocations and (d) the fraction of debonded interfaces; the initial hydrogen concentration in NILS throughout the specimen before loading in this case was 1.0 appm. By comparing Figs. 7b–d, the importance of the effective stress in configuring the interfacial strength is readily apparent. The distribution of hydrogen trapped at dislocations follows that of the effective plastic strain. We emphasize that the fraction of failed interfaces is a result of a complex interaction between the reduction in fracture strength brought about by the trapped hydrogen, the decohesion caused by the principal normal stress, and the effective shear stress acting

Table 2
Decohesion-model related parameters.

		Reference
γ_s (J/m²)	1.95	Hirth and Lothe (1982)
γ_i (J/m²)	0.78	Hirth and Lothe (1982)
Δh_s (kJ/mol)	−95.5	Hirth (1980)
Δh_i (kJ/mol)	−18	Current work
Δs_s (J/mol K)	15	Rice and Wang (1989)
Δs_i (J/mol K)	25	Rice and Wang (1989)
Δg_s (kJ/mol)	−100.0	Calculated at 298 K
Δg_i (kJ/mol)	−25.5	Calculated at 298 K

Table 3
Material parameters.

| Parameter	Value	Reference
Partial molar volume of hydrogen V_H (m³/mol)	2.0×10^{-6}	Hirth (1980)
Metal density V_M (m³/mol)	7.11×10^{-6}	Davis (1998)
Lattice site density N_L (atoms/m)	8.46×10^{-28}	$N_L = V_M/N_A$
Lattice parameter a (m)	2.8865×10^{-10}	Davis (1998)
Trapping sites per trap $\alpha^{(d)}$, $\alpha^{(gb)}$	1.0	Model assumption
Trapping sites per trap $\alpha^{(c)}$	9.09×10^{12}	Model assumption
Lattice sites per solvent atom β	1.0	bcc lattice
Dislocation-related trap density in the undeformed material $N_T^{(d)}$ (m⁻³)	8.5×10^{20}	Kumnick and Johnson (1980)
Grain boundary density $N_T^{(gb)}$ (m⁻³)	10^{23}	Hirth (1980)
Carbide density $N_T^{(c)}$ (m⁻³)	5.5×10^{11}	Current work
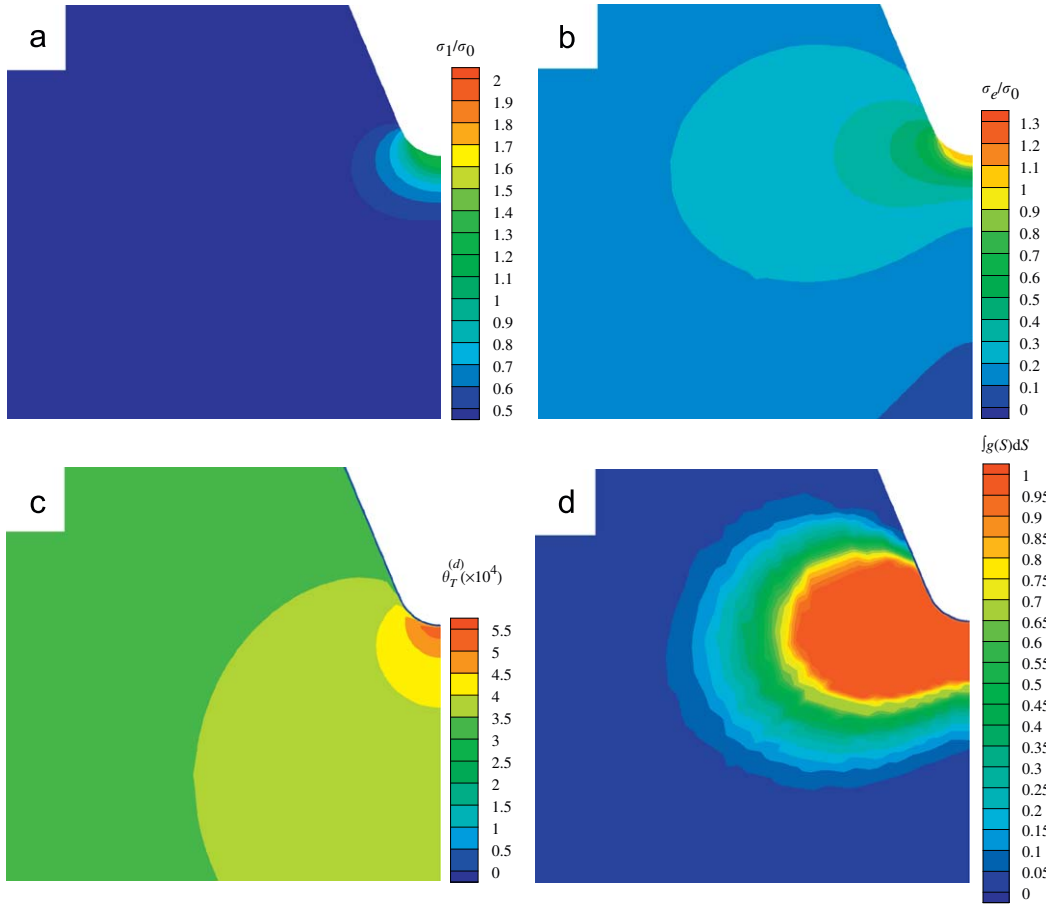
Fig. 7. Results of the finite element computations showing contour plots at the moment of specimen failure of (a) interface strength, (b) effective stress, (c) occupancy of sites for hydrogen trapped at dislocations, (d) fraction of debonded interfaces. The initial hydrogen concentration in NILS is 1.0 appm.
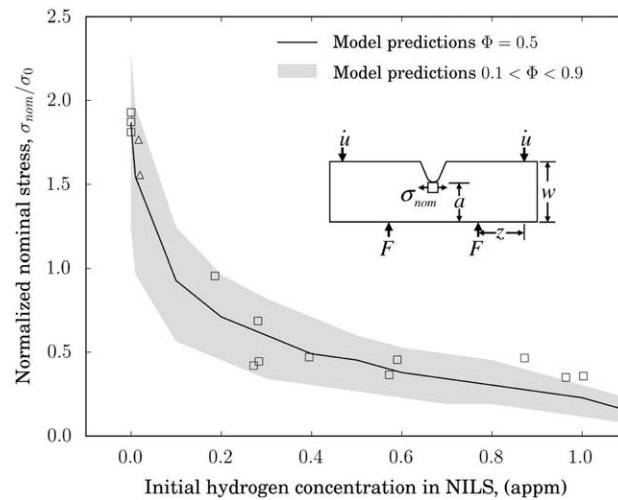

Fig. 8. Model predictions of the fracture strength, measured in terms of the normalized nominal bending stress σ_{nom}/σ_0, plotted against the initial NILS hydrogen concentration in the specimen at the beginning of testing. The superposed experimental data were obtained at a displacement rate of $\dot{u} = 0.1\,\mu\text{m/s}$; the stress opposing the dislocation motion was taken equal to $\tau_0 = 76.9\,\text{MPa}$ which is 0.1% of the shear modulus.

on dislocations and piling them up against carbides. This can be recognized by the fact that whereas the maximum principal stress responsible for opening up the interface attains its peak at the notch root (Fig. 7a), owing to the absence of widespread plasticity as shown in Fig. 3b, there is a substantial combined effect between the effective stress and hydrogen reducing the interfacial strength that results in a widespread zone of failed particles (Fig. 7d). Further, we note that the magnitude of the hydrogen concentration trapped at dislocations is about four orders of magnitude less than the NILS concentrations. The reason is that there are more lattice atoms per unit volume than trapping sites associated with dislocations, $\beta N_L = 8.46 \times 10^{28}$ lattice sites/m^3, as compared with $\alpha^{(d)} N_T^{(d)} = 8.5 \times 10^{20}$ trapping sites at dislocations per m^3 in the undeformed material. According to the present model of fracture, it is the location of hydrogen that controls the fracture event rather than the absolute magnitude of hydrogen away from the fracture site.

Fig. 8 shows the final model predictions for the fracture strength measured in terms of the normalized nominal bending stress σ_{nom}/σ_0 as a function of the initial NILS hydrogen concentration measured in appm, which is equivalent to $10^6 \times c_L^0$ where $c_L^0 = C_L^0/N_L$ (in units of hydrogen atoms per metal atom), in the specimen just before loading was applied. These predictions were calculated with the stress opposing the dislocation motion taken to be equal to $0.001\,\mu = 76.9$ MPa, where μ is the shear modulus. Superposed on the figure are also the experimental data obtained at a crosshead displacement of 0.1 μm/s. It is apparent that the model successfully predicts the hydrogen effect on fracture, specifically in terms of the degradation in fracture strength with hydrogen concentration.

Simulation studies of the parameter sensitivity of the model predictions are given in Appendix C.

6. Discussion

In this work, we have attempted to capture in quantitative and predictive terms the essential elements of hydrogen embrittlement associated with (nominally) brittle intergranular fracture in high-strength steels. This has involved identifying the basic microscopic mechanisms that precede the critical fracture event and their relationship to the characteristic features of the microstructure, quantifying the concentration of hydrogen throughout the process from charging to mechanical testing both as interstitial lattice and trapped hydrogen, computing the effect of such hydrogen on the reversible work of fracture and hence the effective fracture energy, presenting this ensemble in terms of a statistical micro-mechanistic model of hydrogen-assisted fracture, and using this description to quantitatively and accurately predict the experimentally measured degradation in fracture strength with increasing hydrogen concentration in an AISI 4340 high-strength steel.

The statistical approach is important as it provides the link between the statistical distribution of microstructural features, e.g., the size distribution of the grain-boundary carbides, the local probability of their failure, and the development of macroscopic fracture. Moreover, from a mechanistic perspective, the analysis predicts an interesting, perhaps even surprising, effect. In the presence of hydrogen, the locally stress-controlled fracture process can be modeled as the result of three major sequential microscopic events: (i) a dislocation pile-up against a grain-boundary carbide, leading to (ii) interface failure (or cracking) of the carbide, which in turn promotes (iii) decohesion along the grain boundary and hence intergranular fracture. All three events are potentially accelerated by the presence of hydrogen: the dislocation pile-up by hydrogen-enhanced local plasticity (HELP) and the carbide/matrix interface and grain-boundary separations by hydrogen-induced decohesion. However, as the grain boundaries and carbides remain fully H saturated throughout loading regardless of the initial hydrogen content, events (ii) and (iii) cannot be controlling and directly account for the observed degradation in fracture strength with internal hydrogen concentration. Accordingly, we conclude that the critical event in causing hydrogen-induced intergranular fracture is associated with the lowest binding energy trap site, i.e., dislocations, whose hydrogen population varies during loading of the specimen toward failure. As noted, hydrogen trapped at the dislocations reduces their repulsive interactions (Sofronis and Birnbaum, 1995; Robertson, 2001); this increases the number of dislocations in the pile-up thereby intensifying the stress generated when it impinges on the carbide/matrix interface; this in turn deposits hydrogen directly into the interface, reducing the reversible work of decohesion there as it becomes embedded in the dislocation atmosphere. What is satisfying about this description is that it presents a synergistic interaction between the HELP and decohesion mechanisms of hydrogen embrittlement in the development of hydrogen-induced intergranular fracture.

Finally, we note that as appropriate metallic materials that are immune to hydrogen embrittlement are unlikely to be found, the use of structures and components in the presence of hydrogen must involve the use of fracture control plans where damage is monitored or predicted throughout life, akin to the control of fatigue failures using stress-life and/or damage-tolerant methodologies in aircraft structures. Our analysis presents a means to accurately compute the dissolved hydrogen concentration as a function of the history of our samples, and the model itself provides an accurate quantitative description of how this internal hydrogen concentration affects the stress to cause fracture of these samples under mechanical loading. Although the model is presently focused on notched samples, with a similar consideration of crack-tip fields it is readily adaptable to crack-based components. In either case, our approach considers the interplay between the stress gradient and the local probability of finding a "weakest link" (Lin et al., 1986), i.e., it predicts the characteristic distance associated with the onset of the first local fracture event. As such, we believe that our analysis could be used as part of an efficient prognosis procedure to assess the evolution of damage and predict the onset of macroscopic fracture in structures and components subjected to the presence of hydrogen.

7. Conclusions

A physical-based statistical micro-mechanical model has been presented for the intergranular embrittlement of a high-strength low alloy steel due to the presence of dissolved hydrogen. The model is formulated on a quantitative mechanics description of how hydrogen affects the local stress-controlled fracture events, which are related in statistical terms to the characteristic features of the microstructure and to computations of the internal interstitial and trapped hydrogen concentration from charging to mechanical testing. We postulate that the critical role of hydrogen is associated with the motion of dislocations (the lowest binding energy hydrogen trap site), specifically in promoting pile-ups against grain-boundary carbides and enhancing the stress there to cause carbide/matrix interfacial and grain-boundary decohesion, a model that represents a synergistic interplay of the HELP and decohesion mechanisms for hydrogen-assisted fracture.

Under these assumptions of hydrogen-induced fracture driven by dislocation pile-up induced decohesion, and given experimental insight into the hydrogen trapping sites and binding energies, we believe that our approach provides an accurate quantitative prediction of the degradation in fracture stress with increasing internal hydrogen concentration. Moreover, since it embodies a consideration of the interplay between the stress gradient and the local probability of finding a "weakest link", by using appropriate crack-tip fields, our model is readily applicable to crack-based components and thus could be used as a basis for prognosis procedures to predict the potential failure of structural components in the presence of hydrogen.

Appendix A. Thermal desorption analysis

The trap sites and binding energies for hydrogen in the tempered 4340 steel were determined using thermal desorption analysis (TDA), as reported by Sofronis et al. (2009). Hydrogen was dissolved into small blocks of the 4340 steel ($25 \times 13 \times 6.3$ mm^3) by exposing the steel to hydrogen gas at 97 MPa and 85 °C for 210 h. The hydrogen-charged blocks were then individually inserted into a gas chromatograph-type TDA instrument, and each block was heated at a constant rate of 50, 100 or 200 °C/h (up to 600 °C) to evolve hydrogen in a controlled manner. Similar TDA analyses were conducted on blocks of as-tempered steel (i.e., uncharged), which were twice as thick (13 mm) as the hydrogen-charged blocks. The TDA spectra produced at the three different controlled heating rates are shown in Figs. 9a and b for the hydrogen-charged and as-tempered 4340 steels, respectively. The total concentrations of hydrogen from the hydrogen-charged and as-tempered steels were 1.62 and 0.23 wppm, respectively.

One of the challenges encountered in evaluating TDA data is identifying the individual desorption rate peaks in a spectrum. Since desorption rate peaks in TDA spectra have varying breadth and height, it is possible for some peaks to obscure or completely mask others. For the hydrogen-charged 4340 steel, Fig. 9a shows a prominent desorption rate peak in the range 125–190 °C. This low-temperature peak overlaps with a separate peak positioned near 415 °C in the spectrum generated at the heating rate of 200 °C/h. The high-temperature peak becomes more distinct as the heating rate decreases. In addition to the high-temperature peak, there appears to be another peak at intermediate temperatures that is mostly obscured by the prominent low-temperature peak at all heating rates. Evidence for this intermediate-temperature peak is given by subtle perturbations in the flanks of the low-temperature peaks in the temperature range 265–325 °C. The presence of an intermediate-temperature peak is confirmed by examining TDA spectra from the as-tempered 4340 steel. These TDA spectra are shown in Fig. 9b and reveal a distinct peak in the temperature range 265–325 °C. The spectra in Fig. 9b also display the high-temperature peak observed in spectra for the hydrogen-charged steel (Fig. 9a). This consistent presence of the high-temperature peak provides some confidence in the reliability of the data for the as-tempered steel. The interpretation of the TDA spectra for the as-tempered steel is that residual hydrogen, introduced during material processing, is retained in two high-binding energy trap sites, leading to two peaks in the TDA spectra at higher temperatures. The TDA spectra for the as-tempered steel do not exhibit a low-temperature peak, since the trap site associated with this peak has a relatively low binding energy and releases its hydrogen over time.

Based on the above evaluation of the TDA spectra in Fig. 9, three hydrogen desorption rate peaks and associated trap sites are identified for the 4340 steel. According to the analysis of Choo and Lee (1982), the activation energy W_d for each
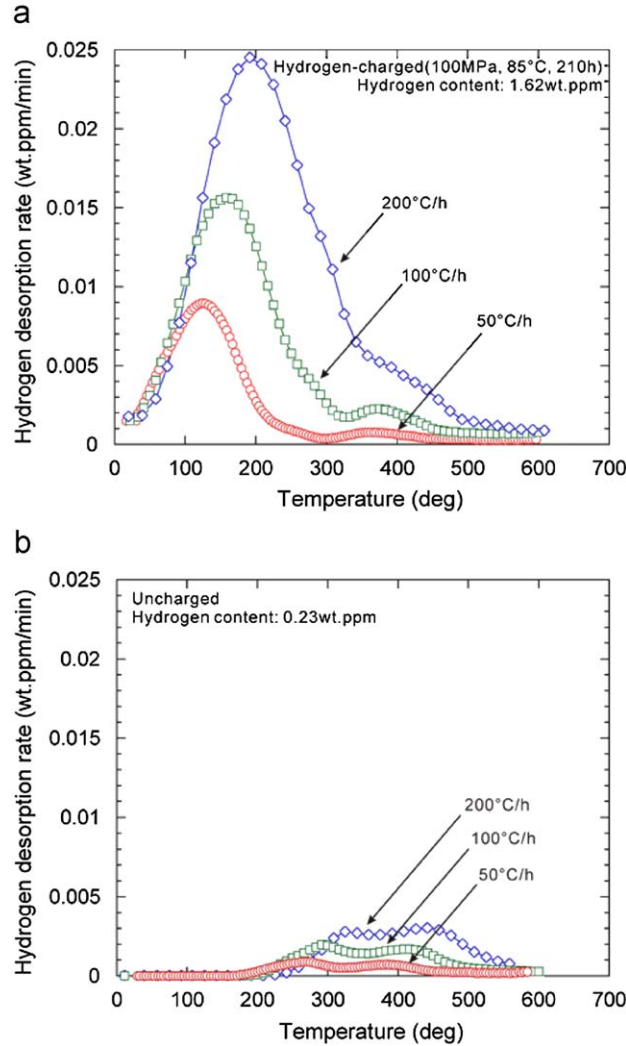
Fig. 9. Thermal desorption analysis spectra from (a) hydrogen-charged and (b) as-tempered (i.e., uncharged) 4340 steel for three different controlled heating rates: 200, 100 and 50 °C/h.

trapping site satisfies

$$\frac{\partial \ln(\alpha/T_c^2)}{\partial(1/T_c)} = -\frac{W_d}{R} \tag{12}$$

where $\alpha = dT/dt$ is the applied heating rate and T_c the absolute temperature corresponding to the desorption rate peak. Using Fig. 9 to identify the temperature T_c corresponding to the maximum desorption rate in each peak and plotting $\ln(T_c^2/\alpha)$ vs. $1/T_c$ as illustrated in Fig. 10, we calculate the activation energy for both the hydrogen-charged and as-tempered steels from the slope of the line fit to the data-points for each individual trap site The T_c values for the second desorption rate peak (i.e., peak at intermediate temperatures) could only be reliably determined from TDA spectra for the as-tempered steel. The T_c values for the third peak (i.e., peak at high temperatures) were identified from spectra for both the hydrogen-charged and as-tempered steels, and Fig. 10 shows that the collection of $\ln(T_c^2/\alpha)$ vs. $1/T_c$ data for this third peak has a consistent trend.

From Fig. 10, the activation energies of desorption for the three trap sites are calculated as 25, 55 and 79 kJ/mol. Given that the activation energy for hydrogen diffusion in iron and low-alloy martensitic steel is ~7 kJ/mol (Nelson and Stein, 1973), the trap binding energies in the 4340 steel are estimated (Choo and Lee, 1982) as 18, 48 and 72 kJ/mol, respectively.

The trap sites associated with the measured binding energies in 4340 are deduced from results from other studies. In particular, Li et al. (2004) determined the trap sites and binding energies for hydrogen in the secondary-hardening martensitic steel AERMET 100 using thermal desorption methods. Similar to the 4340 examined here, the tempered AERMET 100 exhibited three trap sites with widely varying binding energies of about 11, 61 and 89 kJ/mol. The trap sites
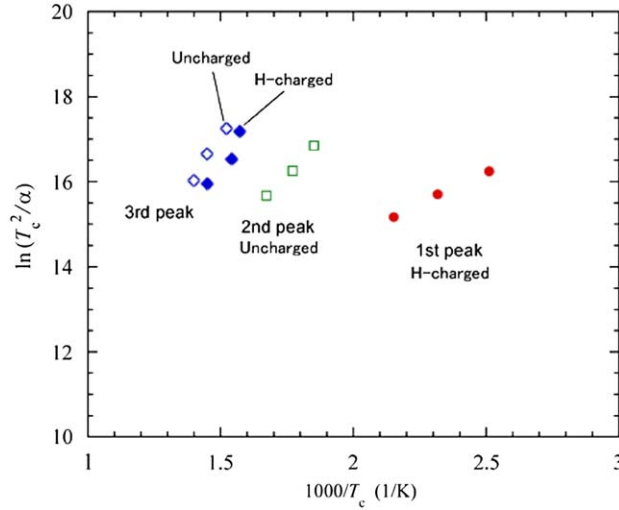
Fig. 10. Plots of $\ln(T_c^2/\alpha)$ vs. $1/T_c$ for the three hydrogen desorption rate peaks in the TDA spectra from Fig. 9 for both the hydrogen-charged 4340 steel as well as the as-tempered (i.e., uncharged) steel. The parameter α is the applied heating rate and T_c the absolute temperature corresponding to the desorption rate peak. According to Eq. (12), the slope of the line through each set of data-points yields the activation energy for desorption of the trap site associated with each peak.

having the two highest binding energies were associated with martensite interfaces, prior austenite grain boundaries, and mixed dislocation cores (61 kJ/mol) and metal carbides (89 kJ/mol). These microstructural features are also present in the tempered 4340 martensitic steel, so it seems reasonable to associate the two high-binding energy trap sites in 4340 to these same microstructural features. The differences in binding energies determined from the two studies (61 and 89 kJ/mol for AERMET 100 vs. 48 and 72 kJ/mol for 4340) could be attributed to variations in experimental accuracy and details of the microstructural features. The low-binding energy trap site in tempered AERMET 100 was associated with nanometer-scale, coherent M_2C precipitates. Since 4340 is not designed to be a secondary-hardening martensitic steel with nanometer-scale M_2C precipitates, it is unlikely that the 4340 steel contains such small, coherent carbides particularly at grain boundaries. Alternately, the low-binding energy trap site in 4340 (18 kJ/mol) can be reasonably assigned to the elastic strain field of dislocations (Hirth, 1980; Choo and Lee, 1982; Serra et al., 1997).

Appendix B. Hydrogen outgassing from the moment of charging until loading

As the principal aim of this work was to associate the experimentally determined and theoretically computed fracture stress with a concentration of hydrogen, outgassing simulations were performed to determine the state and concentration of hydrogen in the SE(B) specimens *at the moment of loading*. This involved accurately computing the hydrogen concentration by modeling the effects of gas pressure and temperature history until the mechanical testing began.

Charging was performed at 100 °C for 2 weeks, at which time the sample was assumed to have a uniform lattice hydrogen concentration throughout, equal to the hydrogen concentration predicted by Sievert's law. For martensitic steel (Nelson and Stein, 1973), the hydrogen concentration in the lattice c[7] (in cm³ hydrogen per cm³ metal) is related to the fugacity f of the charging gas (in Pa) through $c = 1.85 \times 10^{-3} \sqrt{f} \exp(-27100/RT)$, where the gas constant is $R = 8.31$ J mol⁻¹ K⁻¹ and the charging temperature $T = 373$ K. Assuming the Abel–Noble equation of state (San Marchi et al., 2007), we relate the fugacity to the pressure through $f = P \exp(Pb/RT)$, where $b = 15.84$ cm³ mol⁻¹ is a constant for hydrogen gas. The charging pressures were 6.9, 34.5, 69 and 138 MPa, which correspond to fugacities of 7.1, 41.1, 98 and 279 MPa. This gave the calculated uniform lattice hydrogen concentrations at the end of the 2-week charging period at 100 °C as 0.47, 1.13, 1.74 and 2.94 appm. The autoclave was cooled to 25 °C for 8 h while the pressure dropped to 80% of the charging pressure at 100 °C. The temperature and pressure were then held constant for a further 8 h, before the specimens were removed to air until testing.

As the smallest dimension of the sample (Fig. 6) is the thickness (~6.4 mm), hydrogen was assumed to diffuse out primarily through the broad faces. Accordingly, outgassing was modeled for the rectangular region defined by the dashed lines in the lower part of Fig. 6. The initial NILS hydrogen concentration throughout the domain was taken to be the uniform lattice concentration at the end of the charging period. Boundary conditions on the dashed lines were zero flux, reflecting the symmetry of the sample. The boundary conditions on the upper and right boundaries were specified concentrations that reflected the cooling and depressurization of the autoclave; they were calculated using Sievert's law for

---

[7] Throughout the manuscript, a lower case c is used to denote concentration measured in hydrogen atoms per metal atom.

Table 4
Lattice hydrogen concentration in the samples from the moment of charging until the onset of mechanical testing. Initial concentration values are the hydrogen concentration predicted by the outgassing study described in Appendix B.

Charging pressure (MPa)	Concentration predicted by Sievert's law at charging pressure (appm)	Concentration after depressurization (appm)	Time between depressurization and beginning of testing (h)	Initial hydrogen concentration at the onset of testing (appm)
137.9	2.94	1.706	37	0.872
137.9	2.94	1.706	32.25	0.964
137.9	2.94	1.706	30.33	1.003
69.0	1.74	1.015	32.5	0.572
69.0	1.74	1.015	31	0.590
34.5	1.13	0.666	48.67	0.271
34.5	1.13	0.666	46.83	0.281
34.5	1.13	0.666	30	0.395
6.9	0.47	0.293	27.67	0.186
6.9	0.47	0.293	5.67	0.285

the instantaneous fugacity and temperature. The pressure of hydrogen surrounding the sample during cooling and depressurization was modeled according to Gay–Lussac's law $P_1/T_1 = P_2/T_2$. Final depressurization was assumed to occur in 10 s immediately before removing the specimens from the autoclave.

With a boundary condition of zero partial pressure of hydrogen assumed for air, the simulation of hydrogen outgassing was then carried out for each individual specimen between the end of depressurization and the beginning of mechanical testing ($\sim$5–48 h).

As hydrogen has a much lower diffusivity in copper than in steel at low temperature – $D = 11.31 \times 10^{-7}$ (m^2/s)exp($-38{,}878/RT$) in copper (Katz et al., 1971) and $D = 2.33 \times 10^{-7}$(m^2/s)exp($-6680/RT$) in iron and martensitic steel (Nelson and Stein, 1973) – specimens were plated with copper to minimize outgassing. The copper was modeled as a 5 μm thick layer with the given diffusivity and no traps; the steel was modeled as having the given diffusivity and three types of traps corresponding to dislocations, grain boundaries, and carbides. In the steel, as mentioned in Section 3, the trap site densities, $\alpha^{(j)}N_T^{(j)}$, were chosen as follows: $\alpha^{(d)}N_T^{(d)} = 8.5 \times 10^{20}$ m^{-3} for dislocations (corresponding to the Kumnick and Johnson trap density model for zero plastic strain), $\alpha^{(gb)}N_T^{(gb)}$=10^{23} m^{-3} for grain boundaries (Hirth, 1980), and $\alpha^{(c)}N_T^{(c)}$=5×10^{24} m^{-3} for carbides (Hirth, 1980). Through these choices for the trap site densities and the experimentally measured binding energies, and with the use of Eq. (5) along with Sievert's law, we predicted the hydrogen content as measured by thermal desorption analysis of a stress-free sample charged at pressure 97 MPa and temperature 85 °C for 210 h (see Appendix A). For the dislocation and grain boundary trapping model, $\alpha^{(d)} = \alpha^{(gb)} = 1$ trap site/trap. In addition, $\alpha^{(c)} = \alpha^{(c)}N_T^{(c)}/N_T^{(c)} = 5 \times 10^{24}/5.5 \times 10^{11} = 9.09 \times 10^{12}$ trap sites per carbide. For the purpose of the simulations, the solubility of hydrogen in copper was assumed to be the same as the solubility of hydrogen in steel.

For charging at a pressure of 138 MPa, the uniform lattice concentration in the specimen was calculated using Sievert's law to be $c_0 = 2.94$ appm at the end of charging at 100 °C. At the end of depressurization, when the specimen was removed from the autoclave, the specimen was calculated to have a uniform NILS hydrogen concentration equal to 58% of c_0. At the beginning of mechanical testing, which took place after 37 h from depressurization, the NILS concentration c_L^0 was 30% of c_0. Table 4 shows the NILS hydrogen concentrations at the moment specimens were removed from the autoclave (second column) and the moment at which straining of the specimen began (fifth column).

We used the calculated hydrogen concentrations at the moment mechanical testing began as initial concentrations throughout the specimen domain for the formulation of the transient hydrogen transport initial/boundary-value problem.

Appendix C. Simulation studies on the parameter sensitivity of the model predictions

C.1. Dislocation resistance in the Smith model of Eq. (4)

Fig. 11a shows model predictions for three different values of the stress τ_0 opposing the dislocation motion at 50% failure probability and loading rate $\dot{u} = 0.1$ μm/s. The model prediction for $\tau_0 = 76.9$ MPa is the one shown in Fig. 8. As the stress τ_0 opposing the dislocation motion decreases, so does the nominal fracture strength σ_{nom} of the specimen. The effect though is rather small for obstacle strengths less than 200 MPa, i.e., less than 0.26% of the shear modulus. Such magnitudes of dislocation resistance are representative only of the dislocation lattice friction stress in a bcc lattice and not of obstacles such as dislocation cell structure or precipitates. With respect to Fig. 11a, it could be argued that any hydrogen effect on reducing the lattice resistance to dislocation motion is not related to any effect on the macroscopic fracture strength. This observation though should not be confused with the shielding mechanism underlying the HELP model for hydrogen embrittlement which is associated with hydrogen-induced reductions of dislocation-obstacle strengths of the order of at least 5% of the shear modulus. Such large reductions derive from the hydrogen-induced shielding of the long-range stress fields of microstructural singularities such as dislocations or carbon interstitials.
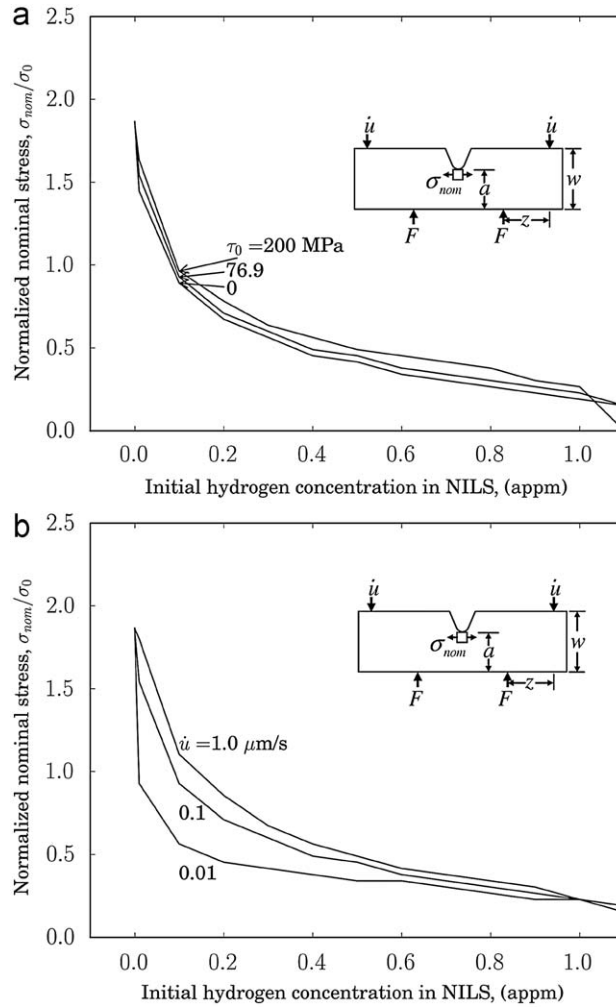
Fig. 11. Model predictions of the fracture strength plotted against the initial NILS hydrogen concentration in the specimen at the beginning of testing for (a) three values of the dislocation-resistance stress τ_0 at a displacement rate of $\dot{u} = 0.1$ m/s and for (b) three different machine displacement rates at a constant dislocation resistance stress $\tau_0 = 76.9$ MPa.

If we consider that $\tau_0 = 76.9$ MPa provides the best fit between model predictions and experimental data (Fig. 8) and that the macroscopic obstacle strength is of the order of the yield strength, i.e., 1490 MPa, then we may deduce from these two values that the hydrogen-induced shielding in the present system is about 1.8% of the shear modulus. We emphasize that such estimates of shielding are an upper bound to any actual shielding as the present Smith model for fracture also predicts the fracture strength on the basis of the hydrogen effect on interfacial cohesion reduction, and not on shielding alone through τ_0.

In summary, the present model is compatible, at minimum qualitatively, with a mechanism of embrittlement in which hydrogen effects on plasticity and decohesion are acting in concert.

C.2. Displacement rate

Fig. 11b shows model predictions at 50% failure probability as a function of the machine displacement rate $\dot{u}$ with the stress opposing dislocation motion set $\tau_0 = 76.9$ MPa. Comparing the model predictions at rates of 0.01, 0.1 and 1.0 μm/s, we notice that the model predicts a smaller fracture strength at lower loading rate. This is in agreement with our understanding that hydrogen-induced fracture is diffusion-controlled. In other words, more hydrogen becomes available by internal redistribution to the fracture initiation sites at slower loading rates than at faster loading rates.

C.3. Dislocation trap density $N_T^{(d)}$

Fig. 10a shows a comparison of the dislocation trap density as a function of the plastic strain according to the work of Kumnick and Johnson (1980) and the trapping model suggested by Sofronis et al. (2001). Kumnick and Johnson, who identified trapping with dislocation debris, calculated the trap density in iron using permeation measurements with deformed iron membranes. In the model of Sofronis et al. (2001), a hydrogen atom is trapped per atomic plane threaded by a dislocation. Lufrano et al. (1998) maintain that this assumption is consistent with the experimental work of Thomas (1980). Thus, the trap density is expressed as a function of the dislocation density ρ and the lattice parameter a: $N_T^{(d)} = \sqrt{2}\rho/a$. For the dislocation density in line length per cubic meter, it was assumed that

$$\rho = \begin{cases} \rho_0 + \gamma \varepsilon^p & \text{for} \quad \varepsilon^p < 0.5, \\ 10^{16} & \text{for} \quad \varepsilon^p \geq 0.5, \end{cases} \tag{13}$$

where ε^p is the effective plastic strain, $\rho_0 = 10^{10}$ line length/m³ denotes the dislocation density for the annealed material, and $\gamma = 2 \times 10^{16}$ line length/m³ (Gilman, 1969). We conclude from Fig. 12a that the dislocation model yields trap densities that are three orders of magnitude larger than those of the Kumnick and Johnson model. For both models, we took the binding energy equal to 18 kJ/mol, as furnished by thermal desorption data (Sofronis et al., 2009) for the specific samples that we tested. However, from Fig. 12b, it is apparent that the model predictions are not sensitive to the trapping model because there is no difference in the normalized failure stress associated either with the dislocation model (larger trap density) or with the Kumnick and Johnson model. The lack of sensitivity of the fracture results to trap densities that are so disparate derives from the fact that the hydrogen-induced decohesion relates to the occupancy of the traps, which are very similar in view of the fact that the binding energy was taken equal to 18 kJ/mol in both models. In addition, trap occupancies in both
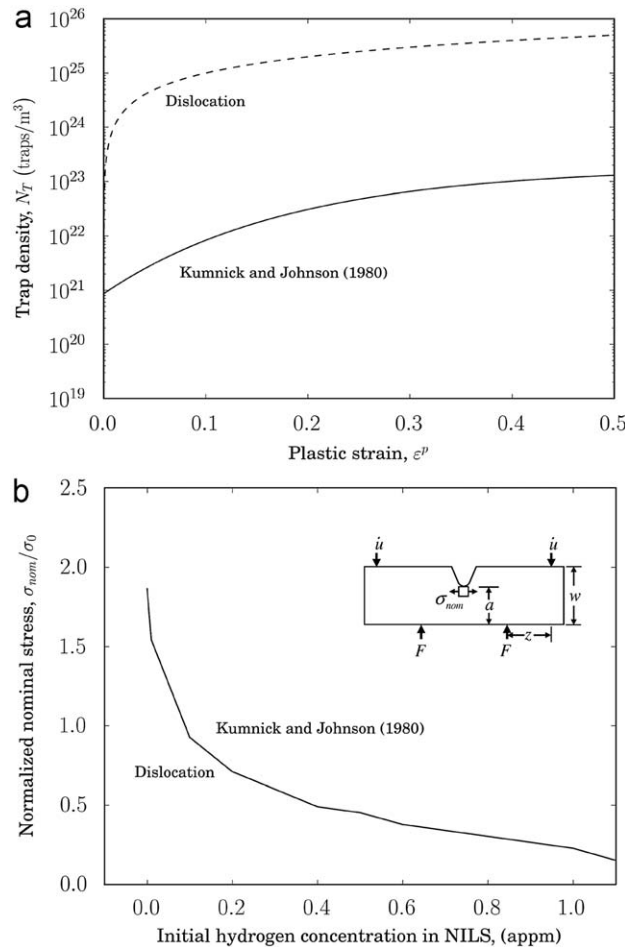

Fig. 12. (a) Trap density vs. effective plastic strain for the dislocation and Kumnick and Johnson trapping models. (b) Prediction of the normalized fracture strength σ_{nom}/σ_0 plotted against the initial NILS hydrogen concentration at the beginning of testing. For both models, the binding energy was 18 kJ/mol, according to thermal desorption measurements.

models are very similar and small ($\sim 10^{-4}$) and the lattice concentrations (appm) are much larger than the trapping concentrations (appb) because the number of NILS, $N_L = 8.46 \times 10^{28}$ sites/m^3, is at least three orders of magnitude larger than the number of trapping sites.

C.4. Relationship between the reversible work and plastic work for decohesion

Eq. (9) is a fundamental relationship of the model that characterizes quantitatively the plastic work expended upon decohesion as function of the corresponding reversible work. Analyzing the competition between the concurrent process of dislocation emission from a crack tip with and crack propagation by atomic bond breaking, Jokl et al. (1980) determined the plastic work for decohesion as a nonlinear function of the reversible work required for bond breaking for a model material system. In view of the fact that experimental data for AISI 4340 steel are lacking, we explored the dependence of the model predictions on the two parameters A and q of the model Eq. (9). We compared the model predictions at which the experimental results are matched well ($A = 0.0216$, $q = 6$) with the predictions of a model ($A = 2.042$, $q = 2$) in which the plastic work is not decreasing as precipitously with decreasing reversible work of fracture as the former. Fig. 13 shows clearly that when this decline is more precipitous, the macroscopic fracture stress decreases because a smaller load is required as the required plastic dissipation accompanying decohesion reduces.

In summary, Fig. 13 demonstrates that that the macroscopic failure load is strongly influenced by the degree of sensitivity of the attendant plastic work of separation on the reversible work of decohesion. As a consequence, hydrogen can markedly affect the fracture mode, even when it affects the reversible work of separation to a small extent.
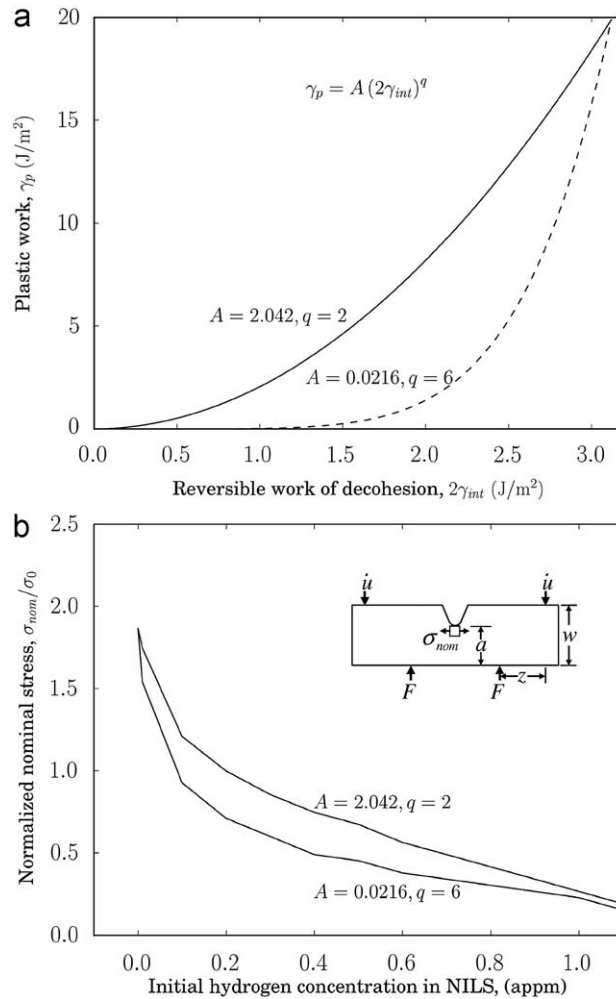

Fig. 13. Model prediction of the normalized fracture strength σ_{nom}/σ_0 plotted against the initial NILS hydrogen concentration in the specimen at the beginning of testing for two models defining the relationship between the reversible work for decohesion and the attendant plastic work.

References

Akhurst, K.N., Baker, T.J., 1981. The threshold stress intensity for hydrogen-induced crack growth. Metall. Trans. A 12A, 1059–1070.

Birnbaum, H.K., Robertson, I.M., Sofronis, P., Teter, D., 1997. Mechanisms of hydrogen related fracture—a review. In: Magnin, T. (Ed.), Corrosion Deformation Interactions CDI'96 (Second International Conference, Nice, France, 1996). The Institute of Materials, UK, pp. 172–195.

Birnbaum, H.K., Sofronis, P., 1994. Hydrogen enhanced localized plasticity—a mechanism for hydrogen related fracture. Mater. Sci. Eng. A 176, 191–202.

Choo, W.Y., Lee, J.Y., 1982. Thermal analysis of trapped hydrogen in pure iron. Metall. Trans. A 13A, 135–140.

Curry, D.A., Knott, J.F., 1978. Effects of microstructure on cleavage fracture stress in steel. Met. Sci. 12, 511–514.

Davis, J.R. (Ed.), 1998. Metals Handbook second ed Materials Park, ASM International, Ohio.

Gangloff, R.P., 2009. Science-based prognosis to manage structural alloy performance in hydrogen. In: Somerday, B., Sofronis, P., Jones, R. (Eds.), Effects of Hydrogen on Materials, ASM International, Materials Park, OH, pp. 1–21.

Gerberich, W.W., Stauffer, D.D., Sofronis, P., 2009. A coexisting view of hydrogen effects on mechanical behavior of crystals: HELP and HEDE. In: Somerday, B., Sofronis, P., Jones, R. (Eds.), Effects of Hydrogen on Materials, ASM International, Materials Park, OH, pp. 38–45.

Gilman, J.J., 1969. Micromechanics of Flow in Solids. McGraw-Hill Book Company, New York, pp. 185–199.

Hirth, J.P., 1980. Effects of hydrogen on the properties of iron and steel. Metall. Trans. A 11A, 861–890.

Hirth, J.P., Rice, J.R., 1980. On the thermodynamics of adsorption at interfaces as it influences decohesion. Metall. Trans. A 11A, 1501–1511.

Hirth, J.P., Lothe, J., 1982. Theory of Dislocations, second ed John Wiley & Sons, New York.

Jokl, M.L., Vitek, V., McMahon, C.J., 1980. A microscopic theory of brittle fracture in deformable solids: a relation between ideal work of fracture and plastic work. Acta Metall. 28, 1479–1488.

Kameda, J., McMahon, C.J., 1980. Solute segregation and brittle fracture in an alloy steel. Metall. Trans. A 11A, 91–101.

Kameda, J., McMahon, C.J., 1983. Solute segregation and hydrogen-induced intergranular fracture in an alloy steel. Metall. Trans. A 14A, 903–911.

Katz, L., Guinan, M., Borg, R.J., 1971. Diffusion of H_2, D_2, and T_2 in single-crystal Ni and Cu. Phys. Rev. B 4, 330–341.

Kumnick, A.J., Johnson, H.H., 1980. Deep trapping states for hydrogen in deformed iron. Acta Metall. 28, 33–39.

Lee, Y., Gangloff, R.P., 2007. Measurement and modeling of hydrogen environment-assisted cracking of ultra-high-strength steel. Metall. Mater. Trans. A 38A, 2174–2190.

Lee, T.D., Goldenberg, T., Hirth, J.P., 1979. Effect of hydrogen on fracture of U-notched bend specimens of quenched and tempered AISI 4340 steel. Metall. Trans. A 10A, 439–448.

Li, D., Gangloff, R.P., Scully, J.R., 2004. Hydrogen trap states in ultrahigh-strength AERMET 100 steel. Metall. Mater. Trans. A 35A, 849–864.

Liang, Y., Sofronis, P., 2003. Micromechanics and numerical modelling of the hydrogen–particle–matrix interactions in nickel-base alloys. Model. Simul. Mater. Sci. Eng. 11 (4), 523–551.

Lin, T., Evans, A.G., Ritchie, R.O., 1986. A statistical model of brittle fracture by transgranular cleavage. J. Mech. Phys. Solids 34, 477–497.

Lufrano, J., Symons, D.M., Sofronis, P., 1998. Hydrogen transport and large strain elastoplasticity near a notch in alloy X-750. Eng. Fract. Mech. 59, 827–845.

McMahon Jr., C.J., Vitek, V., 1979. The effects of segregated impurities on intergranular fracture energy. Acta Metall. 27, 507–513.

McMahon Jr., C.J., Vitek, V., Kameda, J., 1981. Mechanics and mechanisms of intergranular fracture. In: Chell, G.G. (Ed.), Developments in Fracture Mechanics – 2. Applied Science Publishers, London, pp. 193–246.

McMahon Jr., C.J., 2001. Hydrogen-induced intergranular fracture of steels. Eng. Fract. Mech. 68, 773–788.

Moody, N.R., Robinson, S.L., Garrison Jr., W.M., 1990. Hydrogen effects on the properties and fracture modes of iron-based alloys. Res. Mech. 30, 143–206.

Morgan, M.J., 1987. Grain-boundary segregation and embrittlement by antimony and hydrogen in a model alloy steel. Ph.D. Dissertation. University of Pennsylvania, Philadelphia, PA.

Nelson, H.G., Stein, J.E., 1973. Gas-phase hydrogen permeation through alpha iron, 4130 steel, and 304 stainless steel from less than 100 to near 600 °C. NASA Technical Note NASA TN D-7265.

Oriani, R.A., 1970. The diffusion and trapping of hydrogen in steel. Acta Metall. 18, 147–157.

Rice, J.R., Wang, J.-S., 1989. Embrittlement of interfaces by solute segregation. Mater. Sci. Eng. A 107, 23–40.

Ritchie, R.O., Knott, J.F., Rice, J.R., 1973. On the relationship between critical tensile stress and fracture toughness in mild steel. J. Mech. Phys. Solids 21, 395–410.

Robertson, I.M., 2001. The effect of hydrogen on dislocation dynamics. Eng. Fract. Mech. 68, 671–692.

San Marchi, C., Somerday, B.P., Robinson, S.L., 2007. Permeability, solubility and diffusivity of hydrogen isotopes in stainless steels at high gas pressures. Int. J. Hydrogen Energy 32, 100–116.

Serra, E., Perujo, A., Benamati, G., 1997. Influence of traps on the deuterium behavior in the low activation martensitic steels F82H and Batman. J. Nucl. Mater. 245, 108–114.

Smith, J., 1966. The nucleation and growth of cleavage microcracks in mild steel. In: Stickland, A.C. (Ed.), Proceedings of the Conference on Physical Basis of Yield and Fracture. Institute of Physics and Society, Oxford, pp. 36–46.

Sofronis, P., Birnbaum, H.K., 1995. Mechanics of the hydrogen–dislocation–impurity interactions – I. Increasing shear modulus. J. Mech. Phys. Solids 43, 49–90.

Sofronis, P., Dadfarnia, M., Novak, P., Yuan, R., Somerday, B., Robertson, I.M., Ritchie, R.O., Kanezaki, T., Murakami, Y., 2009. A combined applied mechanics/ materials science approach toward quantifying the role of hydrogen on material degradation. In: Proceedings of the 12th International Conference on Fracture, 12 July–17 July (Paper appeared in a conference CD-ROM format). Ottawa, Canada, in press.

Sofronis, P., Liang, Y., Aravas, N., 2001. Hydrogen induced shear localization of the plastic flow in metals and alloys. Eur. J. Mech. A – Solids 20, 857–872.

Sofronis, P., McMeeking, R.M., 1989. Numerical analysis of hydrogen transport near a blunting crack tip. J. Mech. Phys. Solids 37 (3), 317–350.

Taha, A., Sofronis, P., 2001. A micromechanics approach to the study of hydrogen transport and embrittlement. Eng. Fract. Mech. 68, 803–837.

Teter, D.F., Robertson, I.M., Birnbaum, H.K., 2001. The effects of hydrogen on the deformation and fracture of β-titanium. Acta Mater. 49, 4313–4323.

Thomas, G.J., 1980. Hydrogen trapping in FCC metals. In: Thompson, A.W., Bernstein, I.M. (Eds.), Hydrogen Effects in Metals. Transactions of the Metallurgical Society of AIME, New York, NY, pp. 77–85.

Thompson, A.W., Bernstein, I.M., 1977. The role of plastic fracture processes in hydrogen embrittlement. In: Taplin, D.M.R. (Ed.), Fracture 1977: Advances in Research on the Strength and Fracture of Materials. Pergamon Press, New York, pp. 249–254.

Varias, A.G., 2007. On the diffusion in solids under finite deformation. Open Mech. J. 1, 26–28.